Check for updates

Received: 12 September 2022 | Revised: 5 December 2022 | Accepted: 13 January 2023

DOI: 10.1002/nag.3496

RESEARCH ARTICLE

WILEY

Revisiting the empirical particle-fluid coupling model used in DEM-CFD by high-resolution DEM-LBM-IMB simulations: A 2D perspective

Zhixiong Zeng[1,2] | **Jinlong Fu**[3] | **Y. T. Feng**[3] | **Min Wang**[4]

[1]Department of Civil and Environmental Engineering, The Hong Kong University of Science and Technology, China

[2]Laboratoire Navier/CERMES, Ecole des Ponts ParisTech, Paris, France

[3]Zienkiewicz Centre for Computational Engineering, Faculty of Science and Engineering, Swansea University, UK

[4]Fluid Dynamics and Solid Mechanics Group, Theoretical Division, Los Alamos National Laboratory, Los Alamos, New Mexico, USA

Correspondence
Jinlong Fu, Zienkiewicz Centre for Computational Engineering, Faculty of Science and Engineering, Swansea University, Swansea, Wales SA1 8EP, UK.
Email: jinlong.fu@swansea.ac.uk

Abstract

The work investigates the applicability of the unresolved Computational Fluid Dynamics and Discrete Element Method (CFDDEM) technique based on empirical equations for fluid-particle coupling. We first carry out a series of representative volume element simulations using the high-resolution particle-resolved Lattice Boltzmann method and Discrete Element Method (LBMDEM) coupled by an Immersed Moving Boundary (IMB) scheme. Then, we compare the results obtained by both LBMDEM and empirical equations used in unresolved CFDDEM with analytical solutions. It is found that the existing empirical equations used in solving fluid-particle interactions in 2D CFDDEM fail to accurately calculate the hydrodynamic force applied to solid particles. The underlying reason is that the existing empirical models are obtained based on 3D experimental results and thus are not applicable to 2D problems. Based on the simulation results, a new drag coefficient model is then proposed. The estimated drag forces using the new model are compared favourably with the simulated ones, indicating the good performance of the proposed model.

KEYWORDS

computational fluid dynamics, empirical equations, fluid-particle coupling, Lattice Boltzmann method, seepage

1 | INTRODUCTION

Fluid-particle interactions are very common yet complicated processes involved in many geotechnical, chemical and petroleum engineering problems, such as liquefaction analysis, internal/surface erosion, particle migration in filters, submarine landslides, debris or mud flows, fluidised bed, sand production and hydraulic fractures.[1–6] Because of the high cost and technical limitations, detailed microscopic investigations for fluid-particle interactions in laboratory experiments are extremely hard to be conducted. To this end, the computational simulation becomes an alternative way to gain insight into the particle-fluid system.[7–10]

In dealing with the particle-fluid system, macroscopic Euler-Euler approaches, based on the two-fluid model (e.g.[11,12]) are capable of modelling large-scale engineering problems but limited in providing microscopic information on

This is an open access article under the terms of the Creative Commons Attribution-NonCommercial-NoDerivs License, which permits use and distribution in any medium, provided the original work is properly cited, the use is non-commercial and no modifications or adaptations are made.
© 2023 The Authors. *International Journal for Numerical and Analytical Methods in Geomechanics* published by John Wiley & Sons Ltd.

10969853, 0, Downloaded from https://onlinelibrary.wiley.com/doi/10.1002/nag.3496 by Test, Wiley Online Library on [10/02/2023]. See the Terms and Conditions (https://onlinelibrary.wiley.com/terms-and-conditions) on Wiley Online Library for rules of use; OA articles are governed by the applicable Creative Commons License

movement and interaction of particles.[7,13] To address this limitation, various coupled numerical methods have been developed. These include the Computational Fluid Dynamics and the Discrete Element Method (CFDDEM) coupled by empirical equations based on averaging techniques,[2] the high-resolution CFDDEM coupled by the Immersed Boundary Method (IBM)[14]; and the coupled Lattice Boltzmann Method and Discrete Element Method (LBMDEM).[15] Among them, most published examples within the geotechnical and chemical research communities (e.g.[8,4,16–22] have used the CFDDEM coupled by empirical particle-fluid force models, such as Gidapow[2] and Di Felice[23] models. This type of CFDDEM method is also termed the unresolved CFDDEM, in which the size of the local fluid cell used to solve the Navier-Stokes equations is much larger than the sizes of particles making up the solid phase. The flow around each particle is not resolved but volume-averaged within a local cell through solving the locally averaged Navier-Stokes equations. Empirical correlations are necessary to calculate the hydrodynamic forces on the particles using the mean volume fraction and the fluid velocity at the particle location interpolated from the cell nodes.[24]

Although the unresolved CFDDEM has been extensively used for modelling engineering problems for three decades, the primary drawbacks of the employed coupling theory and the averaging technique based empirical hydrodynamic force model have been highlighted since 2000 (e.g.[25,26]). Currently, unresolved CFDDEM models are often calibrated based on the experimentally determined bulk permeability or standard validation tests, but then applied to simulate a very different problem.[6,27–29] In recent years, several researchers have noted that empirical particle-fluid models should be limited to uniformly distributed particle packings and are not valid for heterogeneous systems.[24,30,31] Additionally, the hydrodynamic force is highly dependent on the empirically correlated drag force calculation.[28,32] Akiki et al.[24] obtained a lower drag force using the CFDDEM model than the LBMDEM model while dealing with the particle–fluid interaction in heterogeneous fluidised beds. Similarly, Zhang et al.[32] investigated the particle-fluid interaction in fluidised beds using the unresolved CFDDEM model with the drag force correlations of Gidaspow,[33] Sarkar et al.[34], Cello et al.[35] and Rong et al.[36], and indicated that none of the aforementioned models could accurately predict the experimental segregation degree at different gas velocities. Kanitz and Grabe[28] found that the Di Felice, the Schiller and Naumann, and the modified Schiller and Naumann drag force models resulted in quite different behaviour in the numerical simulation of suffusion, even though they depicted a similar particle settlement in consolidation tests.

In addition to the absence of rigorous validation of these empirical drag models, the unresolved CFDDEM is unable to correctly calculate the hydrodynamic forces in geotechnical applications like pore-scale porosity and permeability due to the requirement of a coarse mesh.[37] Knight et al.[6] found that, compared with a high-resolution immersed boundary method for calculating fluid-particle interaction forces, existing drag models poorly capture the forces on individual particles in the flows with low Reynolds numbers. In these cases, the simulated fluid flow cannot represent the real fluid-particle systems under consideration.[13,24]

In our view, it is still an outstanding issue if the averaging technique based empirical models can accurately describe the particle-fluid interaction at the particle level. Since many of published work have adopted the Gidaspow and Di Felice models in their 2D simulations, we are curious about the accuracy of these empirical drag models and tried to figure out the problem. Thus, we choose to focus on two-dimensional (2D) problems because 2D unresolved CFDDEM simulations are still extensively used to investigate engineering problems, especially for certain fluid-particle systems, due to the limitation of present computing capability. In this work, we will further discuss some potential issues of averaging technique-based fluid-particle coupling models used in the unresolved CFDDEM technique. After the LBMDEM simulations reach stable states, the high-resolution LBMDEM simulations of fluid flows within granular particle packings will be carried out. Then, the stabilised inlet or outlet velocity from LBMDEM simulations and particle volume fraction will be used to calculate the drag forces applied to particles by empirical equations which is the key for fluid-particle coupling in the unresolved CFDDEM technique. Then, we should be able to evaluate the applicability of the empirical coupling models by comparing them with the high-resolution LBMDEM simulations and the analytical solution.

The remainder of this work is organised as follows: Section 2 will briefly introduce the averaging-based empirical equations for solving fluid-particle interaction in the unresolved CFDDEM. Section 3 presents the fundamentals of the high-resolution LBMDEM technique and its coupling theory using the Immersed Moving Boundary (IMB) scheme. It is followed by the detailed introduction of seepage flows in granular materials with various void fractions and particle diameters using high-resolution LBMDEM models in Section 4. The obtained average velocity from LBMDEM simulations is then used to calculate the hydrodynamic force by empirical correlations in the unresolved CFDDEM. A thorough comparison will be made in Section 5 for the hydrodynamic forces obtained by both LBMDEM and existing empirical equations used in unresolved CFDDEM with analytical solutions. Considering the drawbacks of existing models, a new drag force model is proposed in Section 6. Finally, Section 7 will summarise the primary findings of the work.

10969853, 0, Downloaded from https://onlinelibrary.wiley.com/doi/10.1002/nag.3496 by Test, Wiley Online Library on [10/02/2023]. See the Terms and Conditions (https://onlinelibrary.wiley.com/terms-and-conditions) on Wiley Online Library for rules of use; OA articles are governed by the applicable Creative Commons License

2 | FLUID-PARTICLE INTERACTION FORCES IN UNRESOLVED CFDDEM METHOD

The fluid-particle interaction force, also called hydrodynamic force, is typically considered by a combination of a viscous component, called drag force, F_d, and a pressure gradient induced component F_p. The pressure gradient acting across each particle can be well approximated by the global pressure gradient:

$$\mathrm{F_p} = \mathrm{V_p}\nabla \mathrm{P} \tag{1}$$

where V_p is the particle volume and ∇P is the fluid pressure gradient. In unresolved CFDDEM, the drag force F_d can be calculated according to Equations (2) and (3) proposed by Di Felice[23] and Gidaspow,[33] respectively:

$$\text{Di Felice model:}\begin{cases} F_d = \frac{1}{8}C_D\rho_f\pi d_p^2(\mathbf{U}-\mathbf{V})|\mathbf{U}-\mathbf{V}|\varepsilon^{1-\chi} \\ C_D = \left(0.63 + \frac{4.8}{\sqrt{Re_p}}\right)^2 \\ Re_p = \frac{\varepsilon\rho_f d_p|\mathbf{U}-\mathbf{V}|}{\mu} \\ \chi = 3.7 - 0.65\exp\left[-\frac{(1.5-\log_{10}Re_p)^2}{2}\right] \end{cases} \tag{2}$$

where ρ_f is the fluid density, d_p is the diameter of a particle, $\mathbf{U}$ is the fluid velocity at the particle's location, $\mathbf{V}$ is the particle velocity, Re_p is the Reynolds number, C_D is the drag coefficient which depends on Re_p, and $\varepsilon^{-\chi}$ denotes a corrective function accounting for the presence of other particles in the system on the drag force of the particle under consideration.

$$\text{Gidaspow model:}\begin{cases} F_d = \beta V_p(\mathbf{U}-\mathbf{V}) \\ \beta = \begin{cases} 150\frac{\emptyset_p\mu_f}{\emptyset_f d_p^2} + 1.75\frac{\rho_f}{d_p}|\mathbf{U}-\mathbf{V}| & \emptyset_p > 0.2 \\ 0.75C_D^*\frac{\emptyset_f}{D_p}|\mathbf{U}-\mathbf{V}|\emptyset_f^{-2.65} & \emptyset_p \le 0.2 \end{cases} \\ C_D^* = \begin{cases} \frac{24}{Re_p^*}\left[1 + 0.15(Re_p^*)^{0.687}\right] & Re_p^* \le 10^3 \\ 0.44 & Re_p^* > 10^3 \end{cases} \\ Re_p^* = \emptyset_f Re_p \end{cases} \tag{3}$$

where V_p is the volume of particle, μ_f is the fluid viscosity, $\emptyset_p$ is the volume fraction of particle, $\emptyset_f$ is the porosity with $\emptyset_f = 1-\emptyset_p$, C_D^* is the drag coefficient and Re_p^* is the volume-weighted Reynolds number.

3 | PARTICLE-RESOLVED LBMDEM TECHNIQUE

3.1 | Lattice Boltzmann method (LBM)

Unlike conventional CFD, the fluid phase in LBM is treated as a group of (imaginary) particle packages that reside at the lattice nodes. Each particle package includes several particles, such as 9 particles in the commonly used D2Q9 model which is adopted in this work. Both mass and momentum of fluid particles are characterised by the fluid density distribution functions. The fluid flow can be modelled through resolving the particle collision and streaming processes which are described by the Lattice Boltzmann Equation (LBE):

$$f_i(x + \mathbf{e}_i\Delta t, t + \Delta t) - f_i(x, t) = \Omega_i + F_i\Delta t \tag{4}$$

10969853, 0, Downloaded from https://onlinelibrary.wiley.com/doi/10.1002/nag.3496 by Test, Wiley Online Library on [10/02/2023]. See the Terms and Conditions (https://onlinelibrary.wiley.com/terms-and-conditions) on Wiley Online Library for rules of use; OA articles are governed by the applicable Creative Commons License

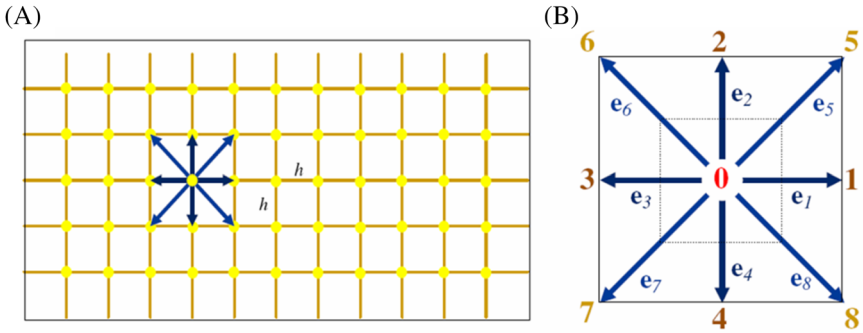

FIGURE 1 LB discretization and D2Q9 model: (A) a standard LB lattice and (B) D2Q9 model

where f_i is the fluid density distribution function in the i direction, x and $\mathbf{e}_i$ are the coordinates and velocity vectors (see Figure 1A) at the current lattice node, and t, Ω_i, and F_i are the current time, collision operator and body force term, respectively. The nine velocity vectors, $\mathbf{e}_i$, in D2Q9 (see Figure 1B) are defined as

$$e_{\mathrm{i}} = \begin{cases} (0,\ 0)\ (\mathrm{i} = 0) \\ \mathrm{C}\left(\cos\frac{\pi(i-1)}{2},\ \sin\frac{\pi(i-1)}{2}\right)\ (\mathrm{i} = 1, \dots, 4) \\ \sqrt{2}\mathrm{C}\left(\cos\frac{\pi(2i-9)}{4},\ \sin\frac{\pi(2i-9)}{4}\right)\ (\mathrm{i} = 5, \dots, 8) \end{cases} \tag{5}$$

in which C is the lattice speed which can be described using the lattice spacing h and time step Δt:

$$C = h/\Delta t \tag{6}$$

There are mainly two collision operators available: the single relaxation time Bhatnagar-Gross-Krook (BGK) and multiple relaxation time (MRT) collision operators. In this work, only the BGK model will be used, where Ω_i is characterised by a relaxation time τ and the equilibrium distribution functions $f_i^{\mathrm{eq}}(x, t)$:

$$\Omega_{\mathrm{i}} = -\frac{\Delta t}{\tau}\left(\mathrm{f_i(x,\ t)} - f_{\mathrm{i}}^{\mathrm{eq}}(\mathrm{x}, t)\right) \tag{7}$$

Additionally, for the D2Q9 model, $f_i^{\mathrm{eq}}(x, t)$ is defined as follows:

$$f_i^{\mathrm{eq}} = \omega_i \rho \left(1 + \frac{3}{C^2}\mathbf{e}_i \cdot \mathbf{u} + \frac{9}{2C^4}(\mathbf{e}_i \cdot \mathbf{u})^2 - \frac{3}{2C^2}\mathbf{u} \cdot \mathbf{u}\right) \qquad (i = 0, \dots, 8) \tag{8}$$

where ρ and $\mathbf{u}$ are the macroscopic fluid density and velocity, respectively. ω_i are the weighting factors:

$$\omega_0 = \frac{4}{9} \qquad \omega_{1,2,3,4} = \frac{1}{9} \qquad \omega_{5,6,7,8} = \frac{1}{36} \tag{9}$$

The macroscopic fluid density ρ and velocity v can be calculated using the distribution functions

$$\rho = \sum_{\mathrm{i}=0}^{8} f_i, \qquad \rho\mathbf{u} = \sum_{\mathrm{i}=1}^{8} f_i \mathbf{e}_i \tag{10}$$

The fluid pressure is given by

$$P = C_{\mathrm{s}}^2\, \rho \tag{11}$$

10969853, 0, Downloaded from https://onlinelibrary.wiley.com/doi/10.1002/nag.3496 by Test, Wiley Online Library on [10/02/2023]. See the Terms and Conditions (https://onlinelibrary.wiley.com/terms-and-conditions) on Wiley Online Library for rules of use; OA articles are governed by the applicable Creative Commons License

where C_s is termed the fluid speed of sound and related to the lattice speed C by

$$C_s = C/\sqrt{3} \tag{12}$$

The kinematic viscosity, η, of the fluid is implicitly determined by

$$\eta = \frac{1}{3}\left(\tau - \frac{1}{2}\right)\frac{h^2}{\Delta t} = \frac{1}{3}\left(\tau - \frac{1}{2}\right)Ch \tag{13}$$

3.2 | Fluid–particle coupling

The Immersed Moving Boundary (IMB) scheme[38] is employed in this work to couple the DEM for particle simulations and the LBM for fluid flow simulations, because of its high efficiency in solving fluid-particle interactions, especially for dense particle packings. In order to retain the advantages of LBM, namely the locality of the collision operator and the simple linear streaming operator, an additional collision term, Ω_i^S, for the boundary nodes covered partially or fully by the solid is introduced to the standard collision operator of LBM. The modified collision operator for resolving the fluid-solid interaction in IMB is given by[10]

$$\Omega = -\frac{\Delta t}{\tau}(1-B)\left[f_i(x,t) - f_i^{eq}(x,t)\right] + (1-B)\Delta t F_i + B\Omega_i^S \tag{14}$$

where F_i is the body force and B is a weighting function that depends on the local solid ratio, ε, defined as the fraction of the solid particle area over the nodal area. It should be highlighted that the following weighting function could smoothly represent the solid boundary during movement of particles

$$B = \frac{\varepsilon(\tau - 0.5)}{(1-\varepsilon) + (\tau - 0.5)} \tag{15}$$

When $\varepsilon = 0$, $B = 0$; when $\varepsilon = 1$, $B = 1$. As the effective evaluation of the local solid ratio ε is very important for generating the smoothness and stability of the fluid-moving boundary calculations, for a detailed discussion on this issue can be found in Wang et al.[39]

The additional collision term Ω_i^S is based on the bounce-back rule for the nonequilibrium part

$$\Omega_i^S = f_{-i}(x,t) - f_i(x,t) + f_i^{eq}(\rho, \mathbf{U}_s) - f_{-i}^{eq}(\rho, \mathbf{u}_i) \tag{16}$$

where $\mathbf{U}_s$ is the velocity of the particle under consideration and $\mathbf{u}_i$ is the velocity of the fluid at the node. The resultant hydrodynamic force ($F_{f\text{-}d}$) and torque ($T_{f\text{-}d}$) exerted on the solid particle can be evaluated by

$$F_{f-d} = Ch\left[\sum_n \left(B_n \sum_i \Omega_i^S \mathbf{e}_i\right)\right] \tag{17}$$

$$T_{f-d} = Ch\left[\sum_n (x - x_p)\left(B_n \sum_i \Omega_i^S \mathbf{e}_i\right)\right] \tag{18}$$

Validations of our LBMDEM code can be found in our previous work.[10,39–41]

4 | MODEL SETUP AND TEST CASES

Flow past a cylinder has long been a subject of interest to researchers in fluid dynamics. Extensive work including experiments and numerical simulations has been undertaken. In our simulations, this problem is extended to consider steady flows around circular cylinders placed in a long rectangular channel with pressure and periodic boundary conditions as shown in Figure 2. Predesigned circular cylinders are randomly distributed to represent various porosities. A pressure

10969853, 0, Downloaded from https://onlinelibrary.wiley.com/doi/10.1002/nag.3496 by Test, Wiley Online Library on [10/02/2023]. See the Terms and Conditions (https://onlinelibrary.wiley.com/terms-and-conditions) on Wiley Online Library for rules of use; OA articles are governed by the applicable Creative Commons License

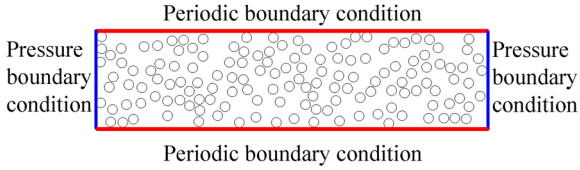

FIGURE 2 Model setup including boundary conditions and initial conditions

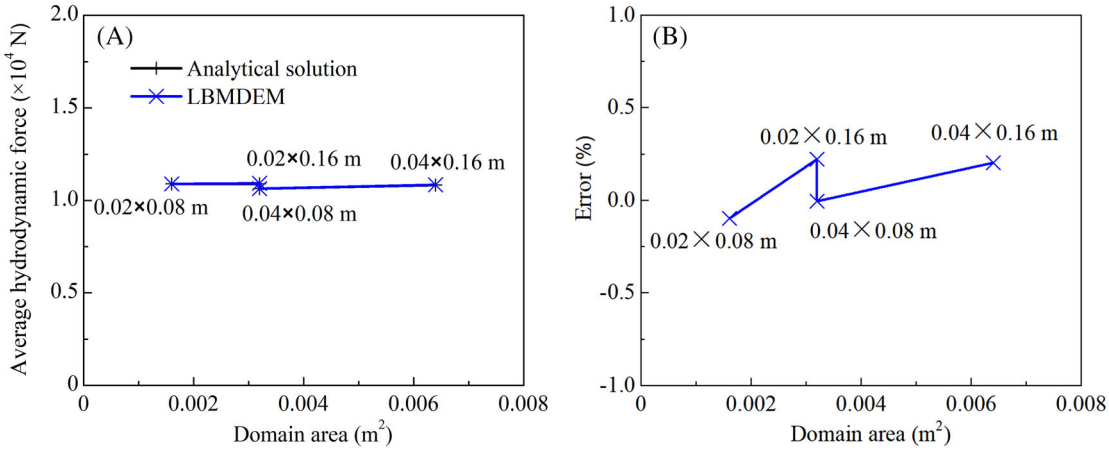

FIGURE 3 Simulated average hydrodynamic force (A) and numerical error (B) for the samples with various domain sizes and under a hydraulic gradient of 0.001

boundary condition is applied at both the inlet (left) and the outlet (right) boundaries of the fluid domain. The periodic boundary conditions (PBC) considering solid particles, fluid flow and fluid–solid interactions are applied to the top and bottom of the computational domain to save the computing time and eliminate the boundary effect. Note that all the granular particles are fixed in this study and the fluid flows within granular particle packings. Physically, the total hydrodynamic force applied to all solid particles can be analytically derived as described below. Let the area of the inlet be A. Based on the applied pressure difference/drop (ΔP) between the inlet and outlet, we can calculate the external force (F_{external}) applied to the fluid is

$$F_{\text{external}} = A\Delta P \tag{19}$$

As the top and bottom of the computational domain are periodic boundaries, the other force influencing the fluid flow is the fluid-particle interaction which is the reaction of hydrodynamic force applied to all solid particles. To reach the equilibrium state of fluid flow, the external force must be equal to the total hydrodynamic force applied to the particle packing. Therefore, the magnitude of the total fluid-particle interaction (also the total hydrodynamic force) at equilibrium can be given by

$$F_{f-d} = A\,\Delta P \tag{20}$$

which essentially states the total hydrodynamic force is equal to the seepage force in the framework of the Darcy flow. Then, the hydrodynamic force applied to each particle can be averaged by the particle number as F_{f-d}/N_{p} where N_{p} is the particle number.

Before conducting the simulation tests, several sensitivity tests are performed to examine the convergence of the coupled LBMDEM used in this work. To clarify the effect of domain size on the simulation results, four tests are conducted on the samples with various domain sizes of 0.02×0.08 m, 0.04×0.08 m, 0.02×0.16 m and 0.04×0.16 m. The constituent particles are 2 mm in diameter and the porosity is 0.800. To further investigate the grid size effect, four fluid cell resolutions with different grid sizes 0.4, 0.2, 0.1, 0.08 and 0.05 are simulated on the sample with a domain size of 0.02×0.08 m. The corresponding grid size ratios (the ratio of particle diameter to grid size) are 5, 10, 20, 25 and 40. The variations of the average hydrodynamic force of each particle with domain area and grid size ratio under a hydraulic gradient of 0.001 are presented in Figures 3 and 4, respectively. As all numerical errors are within 1%, the simulation results using LBMDEM are in good agreement with analytical values regardless of the domain size and grid size.

10969853, 0, Downloaded from https://onlinelibrary.wiley.com/doi/10.1002/nag.3496 by Test, Wiley Online Library on [10/02/2023]. See the Terms and Conditions (https://onlinelibrary.wiley.com/terms-and-conditions) on Wiley Online Library for rules of use; OA articles are governed by the applicable Creative Commons License

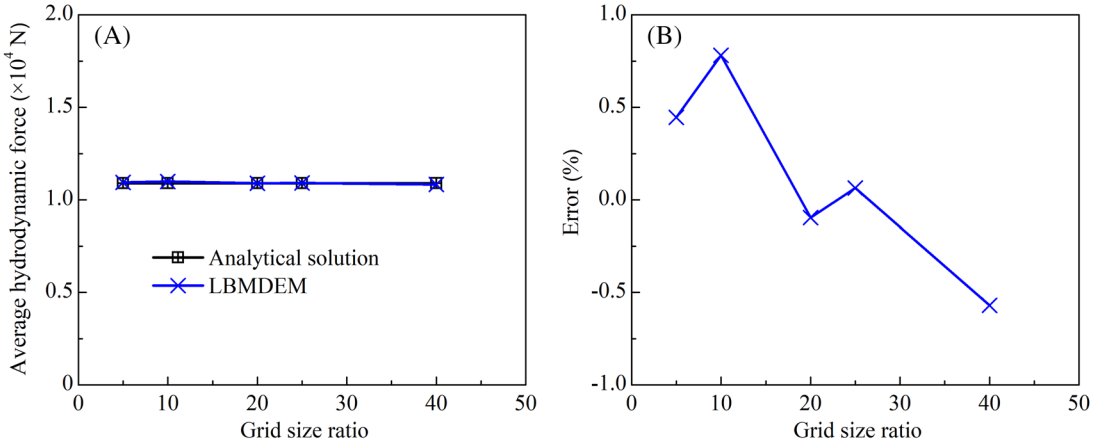

FIGURE 4 Simulated average hydrodynamic force (A) and numerical error (B) for the samples with various grid sizes and under a hydraulic gradient of 0.001

Therefore, the domain of the problem under consideration is selected as 2 cm in height (the Y direction) and 8 cm in length (the X direction). Four (cylindrical) particle packings are generated, and the particles are uniformly distributed within the computational domain. The corresponding porosities are respectively 0.80 for the case with 332 particles, 0.80 for the case with 215 particles, 0.80 for the case with 144 particles and 0.90 for the case with 70 particles (the details are listed in Table 1). To account for the influences of particle size and pressure gradient, 20 more numerical cases with the diameter of the solid particles ranging from 1 to 4 mm and the pressure difference ranging from 0.78 to 7.848 Pa, are carried out (see Table 1 for details). The lattice space, that is, the fluid element size, adopted in the LBM simulations is 0.1 mm and thus the fluid domain is divided into 800×200 elements or grids. The corresponding grid size ratio ranges from 20 to 80, enabling the accurate simulation of seepage force according to Figure 4. The relaxation parameter τ is 0.50005. The contact stiffness and density of particles are 5×10^7 N/m and 2.65 g/cm^3. The fluid density and kinematic viscosity are 1.0 g/cm^3 and 10^{-6} m^2/s.

5 | RESULTS AND DISCUSSION

5.1 | Evolution of fluid flow in granular packings

As we apply a higher pressure at the left boundary (inlet), the fluid will flow from the left to the right once the pressure drop is applied. Figure 5 presents the typical velocity contour in the lattice coordinate system of the sample with a particle diameter of 2 mm under a hydraulic gradient of 0.001. When the fluid flow approaches the front side of the cylinder, the fluid pressure increases and the fluid is forced to move around the cylinder surface. When the Reynolds number increases, the fluid cannot follow the cylinder surface to the rear side but separates from both sides, and a pair of symmetric vortices are formed in the near wake ($t = 0.25$ s). As the Reynolds number further increases, the wake becomes unstable.

The evolution of the average horizontal inlet velocity with the elapsed time for the samples at the particle diameter of 2 mm and various porosities is depicted in Figure 6. The average inlet velocities increase quickly with time and then tend to be stabilised after 0.08, 0.30, 1.68 and 3.42 s for the samples with porosities of 0.53, 0.70, 0.80 and 0.90, respectively.

5.2 | Hydrodynamic force

The total hydrodynamic forces applied on all the particles in each packing at each time step are also recorded and the evolution of the total hydrodynamic force with the elapsed time is illustrated in Figure 7. When the pressure is applied, the total hydrodynamic forces increase quickly and then reach a similar stabilised value of 0.0157, which is the analytic value of the hydrodynamic force caused by the applied hydraulic gradient 0.001.

Table 1 summarises the stabilised average horizontal inlet velocity and total hydrodynamic forces of the samples with various porosities and particle diameters under various hydraulic gradients. The total hydrodynamic forces are also

10969853, 0, Downloaded from https://onlinelibrary.wiley.com/doi/10.1002/nag.3496 by Test, Wiley Online Library on [10/02/2023]. See the Terms and Conditions (https://onlinelibrary.wiley.com/terms-and-conditions) on Wiley Online Library for rules of use; OA articles are governed by the applicable Creative Commons License

TABLE 1 Numerical simulation arrangement

Sample No.	Porosity	Particle diameter (m)	Hydraulic gradient	Velocity (10^{-4} m/s)	Analytical solution		LBMDEM		Gidapow equation		Di Felice equation	
					Hydrodynamic forces (10^{-2}N)	Drag force (10^{-2}N)	Hydrodynamic forces (10^{-2}N)	Drag force (10^{-2}N)	Hydrodynamic forces (10^{-2}N)	Drag force (10^{-2}N)	Hydrodynamic forces (10^{-2}N)	Drag force (10^{-5}N)
1	0.53	0.002	0.001	0.09	1.57	0.83	1.58	0.84	0.74	0	0.74	1.68
2	0.53	0.002	0.01	0.94	15.70	8.30	15.77	8.38	7.40	0.01	7.39	1.72
3	0.53	0.002	0.04	3.77	62.85	33.28	63.10	33.53	29.66	0.09	29.57	1.93
4	0.53	0.002	0.07	6.58	110.09	58.34	110.42	58.67	51.98	0.23	51.75	2.22
5	0.53	0.002	0.1	9.37	156.96	83.03	157.75	83.82	74.33	0.41	73.93	2.55
6	0.70	0.002	0.001	1.86	1.57	1.09	1.58	1.10	0.49	0.01	0.48	0.56
7	0.70	0.002	0.01	17.65	15.70	10.91	15.76	10.98	5.26	0.47	4.79	1.08
8	0.70	0.002	0.04	74.29	62.78	43.63	62.96	43.81	24.50	5.35	19.15	4.73
9	0.70	0.002	0.07	125.84	109.98	76.47	109.89	76.38	46.92	13.41	33.52	10.42
10	0.70	0.002	0.1	166.46	157.27	109.40	156.45	108.58	69.88	22.01	47.89	16.53
11	0.80	0.002	0.001	12.80	1.57	1.25	1.58	1.26	0.47	0.15	0.32	0.41
12	0.80	0.002	0.004	42.62	6.28	5.00	6.30	5.02	2.38	1.10	1.28	1.02
13	0.80	0.002	0.007	66.18	10.99	8.74	11.02	8.77	4.57	2.33	2.25	1.71
14	0.80	0.002	0.01	86.45	15.70	12.49	15.74	12.53	6.89	3.68	3.21	2.45
15	0.90	0.002	0.0001	6.79	0.16	0.14	0.15	0.14	0.04	0.02	0.02	0.11
16	0.90	0.002	0.0004	24.52	0.63	0.57	0.63	0.56	0.24	0.17	0.06	0.21
17	0.90	0.002	0.0007	38.88	1.10	0.99	1.10	0.99	0.48	0.37	0.11	0.31
18	0.90	0.002	0.001	51.20	1.57	1.42	1.57	1.41	0.75	0.59	0.16	0.41
19	0.80	0.001	0.001	3.83	1.57	1.25	1.58	1.26	0.38	0.06	0.32	1.03
20	0.80	0.001	0.004	15.09	6.28	4.99	6.31	5.04	0.20	0.05	0.16	0.09
21	0.80	0.001	0.007	25.75	10.99	8.73	11.04	8.82	3.42	1.20	2.22	1.61
22	0.80	0.001	0.01	35.82	15.70	12.47	15.77	12.60	5.23	2.05	3.17	1.94
23	0.80	0.003	0.001	23.68	1.57	1.25	1.57	1.26	0.55	0.23	0.32	0.37
24	0.80	0.003	0.004	84.70	6.28	5.02	6.27	5.00	3.35	2.09	1.26	1.87
25	0.80	0.003	0.007	141.77	10.99	8.78	10.98	8.77	7.40	5.19	2.21	4.36
26	0.80	0.003	0.01	198.50	15.70	12.54	15.63	12.47	12.65	9.50	3.16	7.89
27	0.80	0.004	0.001	31.51	1.57	1.26	1.56	1.24	0.57	0.26	0.31	0.38
28	0.80	0.004	0.004	98.39	6.28	5.03	6.27	5.03	3.12	1.87	1.25	2.10
29	0.80	0.004	0.007	140.57	10.99	8.81	10.93	8.75	5.73	3.55	2.19	3.91
30	0.80	0.004	0.01	188.99	15.70	12.58	15.57	12.45	9.18	6.06	3.12	6.70

10969853, 0, Downloaded from https://onlinelibrary.wiley.com/doi/10.1002/nag.3496 by Test, Wiley Online Library on [10/02/2023]. See the Terms and Conditions (https://onlinelibrary.wiley.com/terms-and-conditions) on Wiley Online Library for rules of use; OA articles are governed by the applicable Creative Commons License

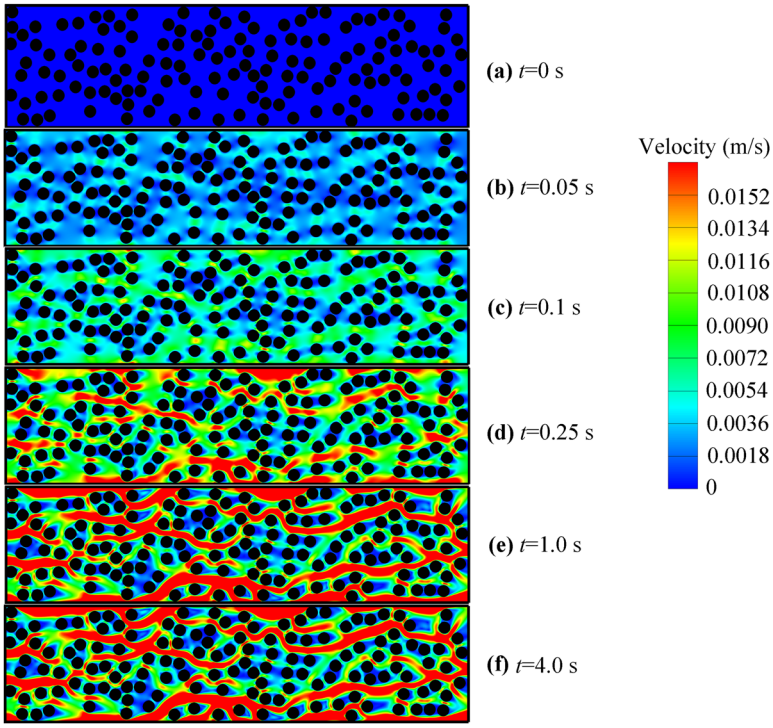

FIGURE 5 Fluid velocity contours at different instants (with porosity 0.80, particle diameter 2 mm, and hydraulic gradient 0.01)

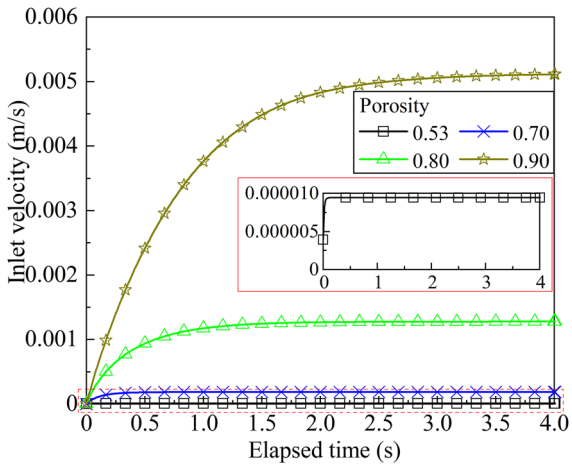

FIGURE 6 Evolution of inlet velocity with elapsed time for the samples with the particle diameter of 2 mm and hydraulic gradient of 0.001

presented in Figures 8 and 9. Overall, the total hydrodynamic force increases linearly with the increase of hydraulic gradient. For comparison, the analytical values are also presented in Figures 8 and 9. For all the samples, the total hydrodynamic forces simulated using LBMDEM match the analytical values well regardless of the porosity and particle diameter, indicating the good accuracy of LBMDEM in the hydrodynamic force calculation.

Each high-resolution LBMDEM simulation can be regarded as a representative volume element model, and is analogous to a single fluid cell in an unresolved CFDDEM simulation. The data in Table 1 give an indication of the applicability of the aforementioned empirical equations for fluid-particle coupling in unresolved CFDDEM. The horizontal velocity around particles is derived from the inlet velocity and porosity of the packing under consideration based on mass conservation. The hydrodynamic forces calculated using Di Felice and Gidaspow equations are presented in Figures 8 and 9. For all the samples with particle diameter of 2 mm, the calculated values using the above two empirical equations are significantly lower than the analytical ones regardless of porosity.

Besides the porosity, the hydrodynamic force calculated from empirical equations is also dependent on the particle diameter. Take the case (see Figure 9) with porosity being 0.795 for example, the calculated hydrodynamic forces using

10969853, 0, Downloaded from https://onlinelibrary.wiley.com/doi/10.1002/nag.3496 by Test, Wiley Online Library on [10/02/2023]. See the Terms and Conditions (https://onlinelibrary.wiley.com/terms-and-conditions) on Wiley Online Library for rules of use; OA articles are governed by the applicable Creative Commons License

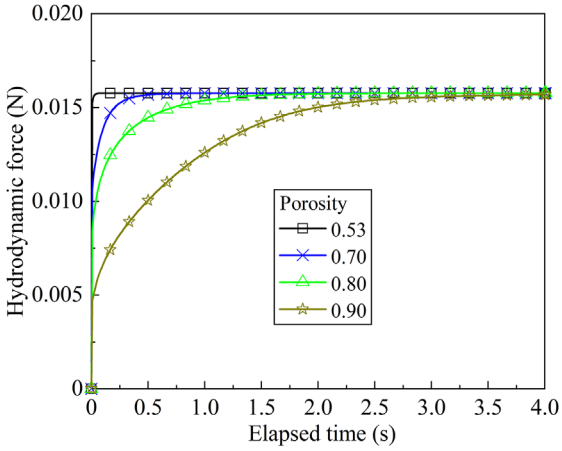

FIGURE 7 Evolution of total hydrodynamic force with elapsed time for the samples with the particle diameter of 2 mm and hydraulic gradient of 0.001

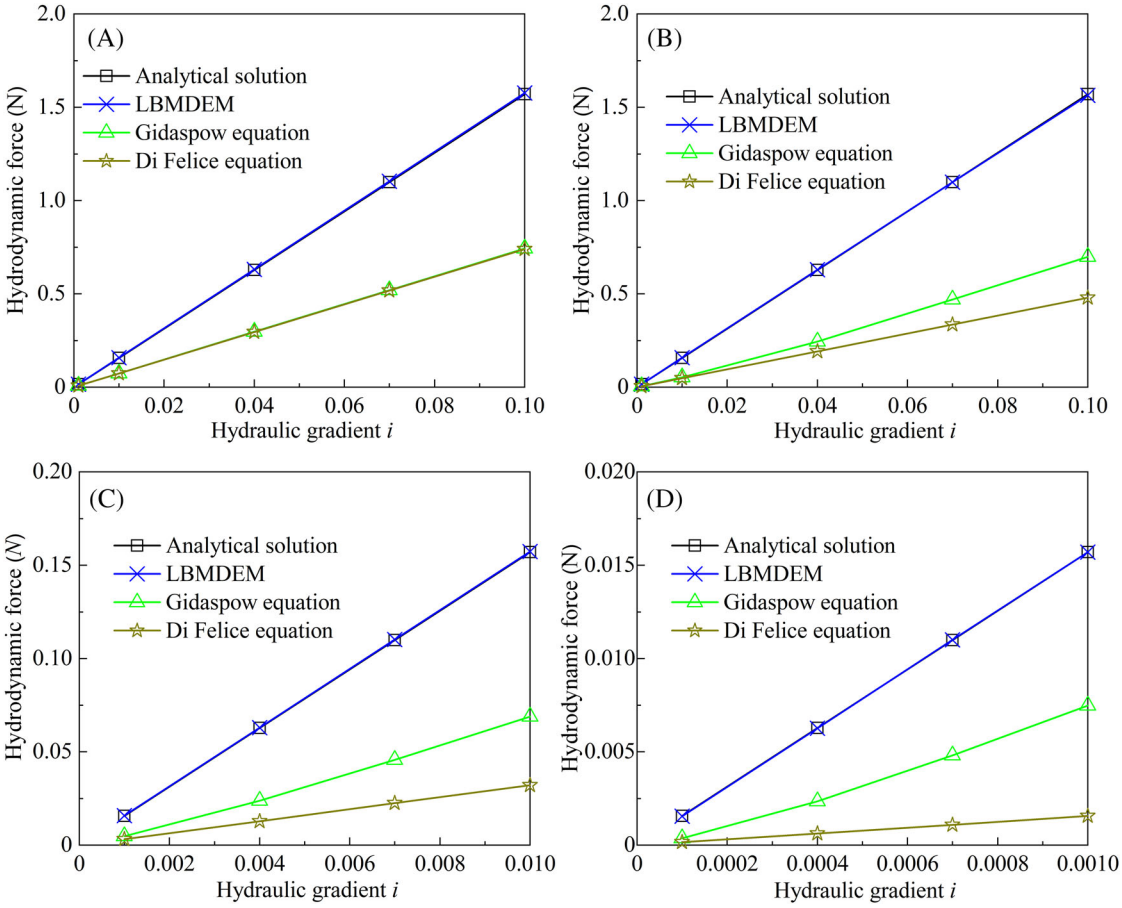

FIGURE 8 Variation of hydrodynamic force with hydraulic gradient for the samples with a particle diameter of 2 mm and various porosities of (A) 0.53, (B) 0.70, (C) 0.80 and (D) 0.90

the Gidaspow equation are generally much lower than the analytical values, and are close to those calculated based on LBMDEM and analytical solution only when the particle diameter is larger than 3 mm. In the unresolved CFDDEM based on empirical equations for fluid-particle interactions, the fluid velocity within a cell is commonly assumed to be constant, and the meso-structure of particle distribution within the granular packing is ignored, such as the leading and trailing edge effects on the left and right boundaries.[42] To further account for these effects, we divide the computational domain

10969853, 0, Downloaded from https://onlinelibrary.wiley.com/doi/10.1002/nag.3496 by Test, Wiley Online Library on [10/02/2023]. See the Terms and Conditions (https://onlinelibrary.wiley.com/terms-and-conditions) on Wiley Online Library for rules of use; OA articles are governed by the applicable Creative Commons License

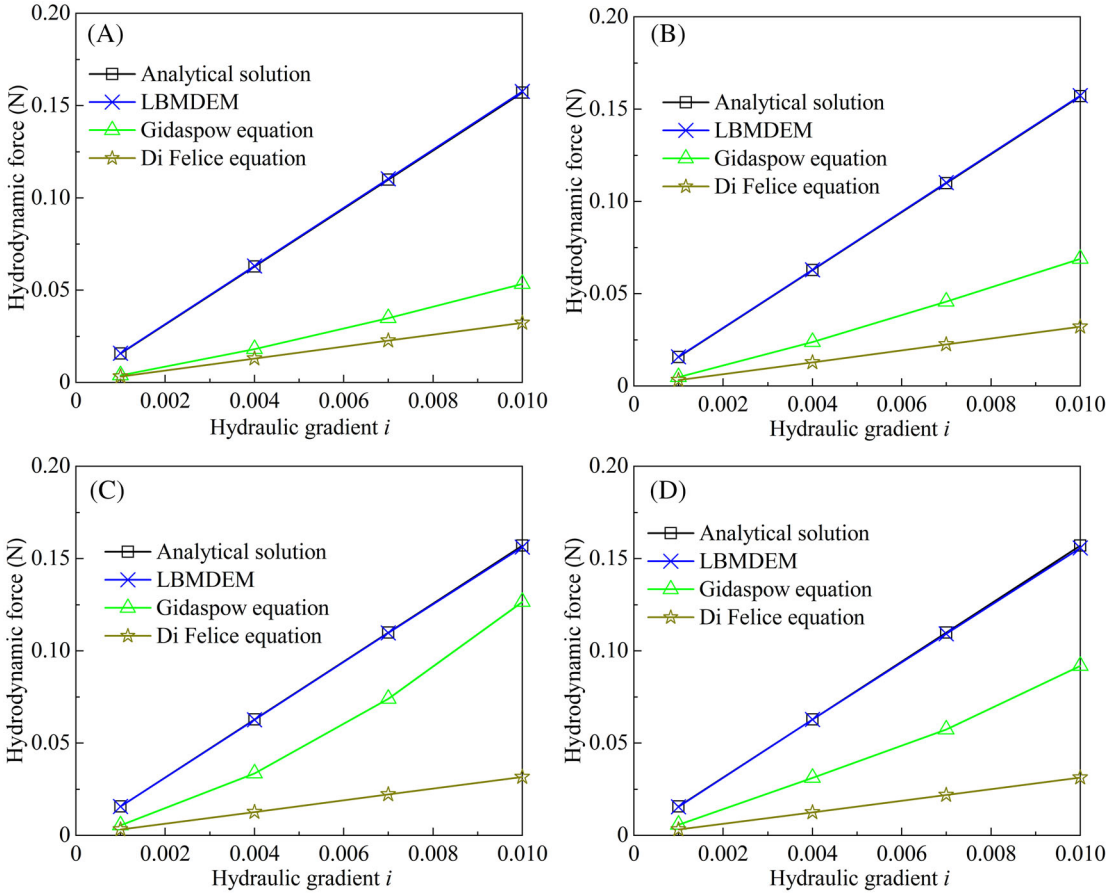

FIGURE 9 Variation of hydrodynamic force with hydraulic gradient for the samples with a porosity of 0.80 and various particle diameters of (A) 0.001 m, (B) 0.002 m, (C) 0.003 m and (D) 0.004 m

into 14 segments along the flow direction, and plot the average hydrodynamic force for particles with their centres in each segment in Figure 10. It can be observed that the hydrodynamic forces are almost the same in the segments except for the leading and tailing ones in the simulations with porosity being 0.53, 0.70 and 0.80. However, there is still a variation of 18% with the hydrodynamic forces along the flow direction apart from the first and the last segments for the loose particle packing with porosity 0.9. This suggests that for the dense particle packings, like the seepage within soil in geotechnical engineering, the averaging may be feasible, but the existing averaging empirical equations are far from sufficient because they do not take the meso-structure of particle packings into account.

To further investigate the influence of porosity on the particle-fluid interaction force, the total hydrodynamic forces of samples with 2 mm diameter under a hydraulic gradient of 0.001 are replotted with porosity in Figure 11. It can be observed that the hydrodynamic forces calculated using LBMDEM and analytical solution are almost constant, regardless of the porosity. With the increase of porosity, the calculated hydrodynamic force by the Di Felice equation decreases. By contrast, the calculated hydrodynamic force by the Gidaspow equation decreases as the porosity is lower than 0.70 and then increases as the porosity is larger than 0.80. This implies that the existing averaging technique based Di Felice and Gidaspow equations cannot accurately calculate the fluid-particle interaction at least for 2 dimensional problems.

Similarly, the variation of hydrodynamic force with particle diameter of samples with a porosity of 0.80 and under a hydraulic gradient of 0.001 is also presented in Figure 12. As the particle diameter increases from 0.001 to 0.008 m, the hydrodynamic forces from both the LBMDEM simulation and the analytical solution remain constant at 0.0157. By contrast, hydrodynamic forces calculated using the Di Felice equation remain constant at 0.0035, while those by the Gidaspow equation increase from 0.0040 to 0.0068.

10969853, 0, Downloaded from https://onlinelibrary.wiley.com/doi/10.1002/nag.3496 by Test, Wiley Online Library on [10/02/2023]. See the Terms and Conditions (https://onlinelibrary.wiley.com/terms-and-conditions) on Wiley Online Library for rules of use; OA articles are governed by the applicable Creative Commons License

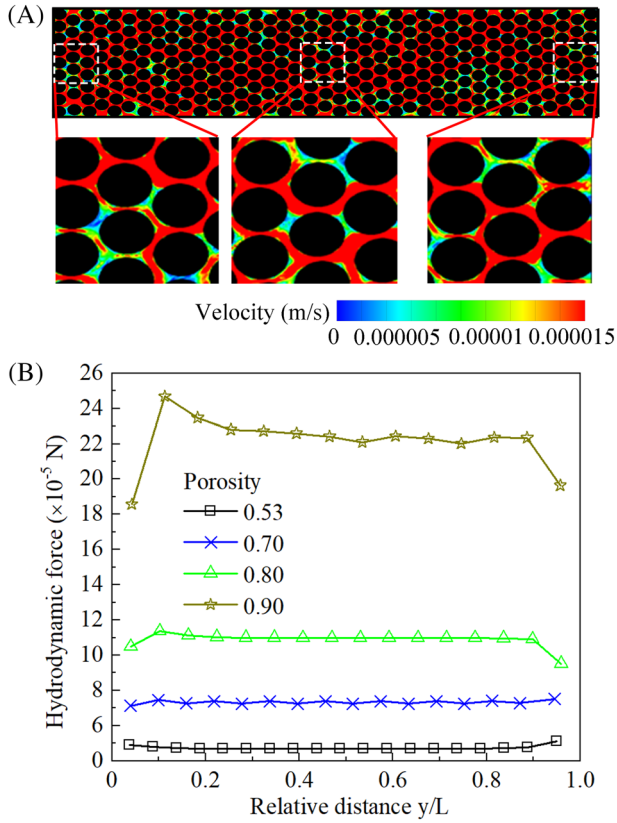

FIGURE 10 Variation of hydrodynamic force along flow direction

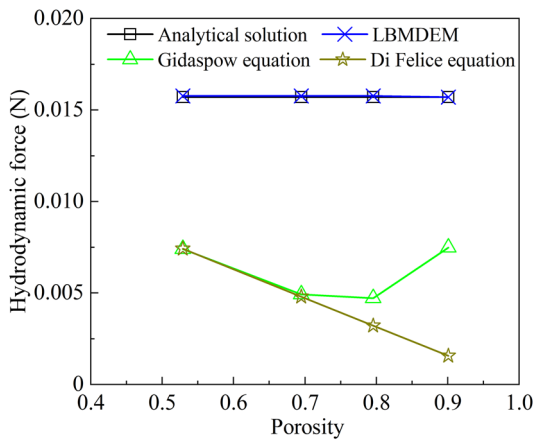

FIGURE 11 Variation of hydrodynamic force with porosity under a hydraulic gradient of 0.001

5.3 | Drag force

As noted above, the particle-fluid interaction force is mainly decomposed into a viscous component F_d and a pressure gradient-induced component F_p. The viscous component results from the friction between the particle and the fluid at the surface of the particle when the fluid velocity is different from the particle velocity.[43] By contrast, the pressure gradient acting across each particle is generally approximated by the global pressure gradient. Note that in LBMDEM simulations, the hydrodynamic force is directly calculated from the momentum exchange between the fluid and the solid particle, and the viscous component and pressure gradient induced component are not separately considered. Thus, the drag force in LBMDEM simulations can be obtained by removing the pressure gradient contribution (see Equation (1)) from the total

10969853, 0, Downloaded from https://onlinelibrary.wiley.com/doi/10.1002/nag.3496 by Test, Wiley Online Library on [10/02/2023]. See the Terms and Conditions (https://onlinelibrary.wiley.com/terms-and-conditions) on Wiley Online Library for rules of use; OA articles are governed by the applicable Creative Commons License

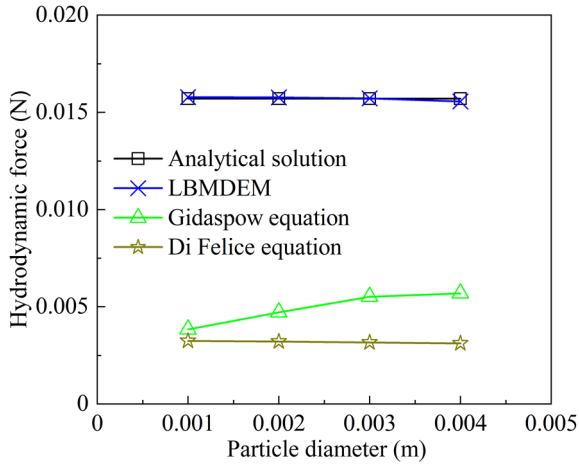

FIGURE 12 Variation of hydrodynamic force with particle diameter of samples with a porosity of 0.80 and under a hydraulic gradient of 0.001

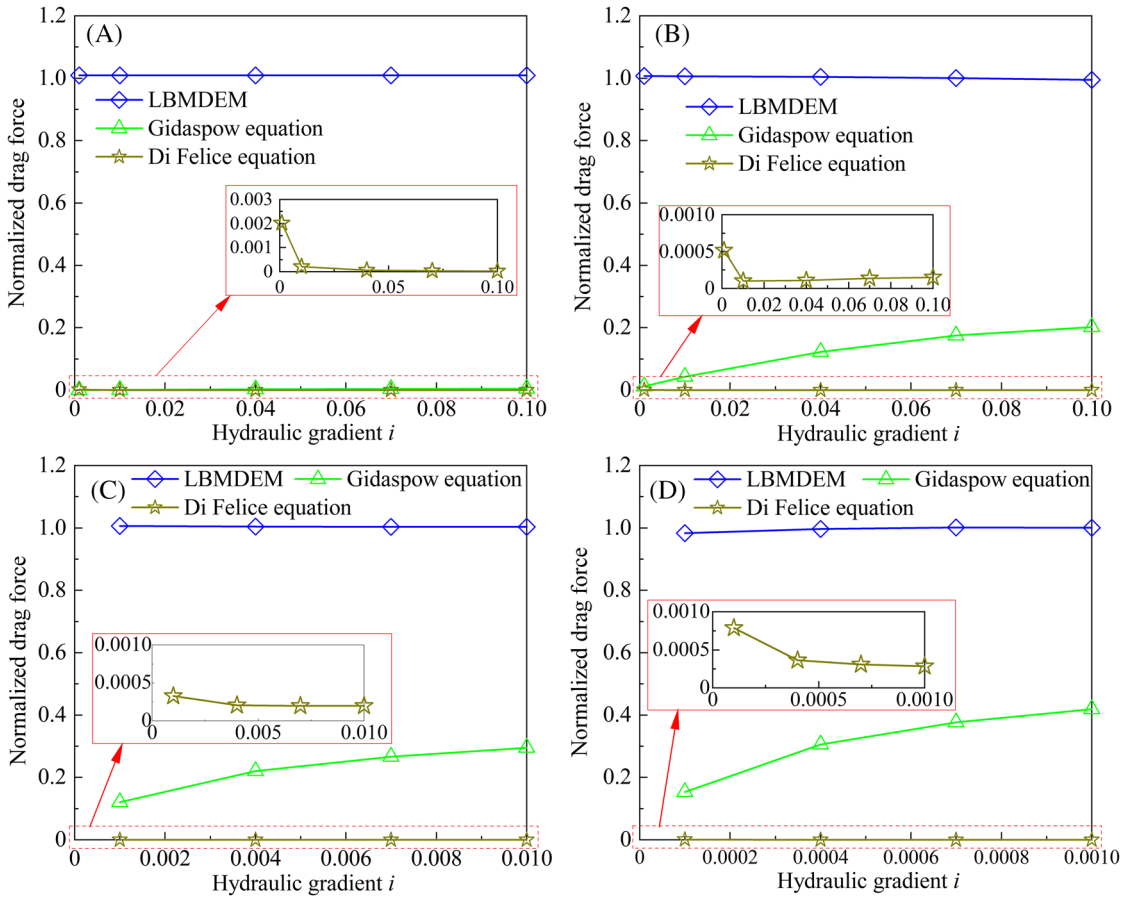

FIGURE 13 Variation of the normalized drag force with hydraulic gradient for the samples with various porosities of (A) 0.53; (B) 0.79; (C) 0.80 and (D) 0.90

hydrodynamic force:

$$F_d = F_{f-d} - F_p \tag{21}$$

The calculated drag force is then normalised using the analytical one. Figures 13 and 14 present the variations of the normalised drag force with hydraulic gradient for the samples with various porosities and particle diameters. It is clear

10969853, 0, Downloaded from https://onlinelibrary.wiley.com/doi/10.1002/nag.3496 by Test, Wiley Online Library on [10/02/2023]. See the Terms and Conditions (https://onlinelibrary.wiley.com/terms-and-conditions) on Wiley Online Library for rules of use; OA articles are governed by the applicable Creative Commons License

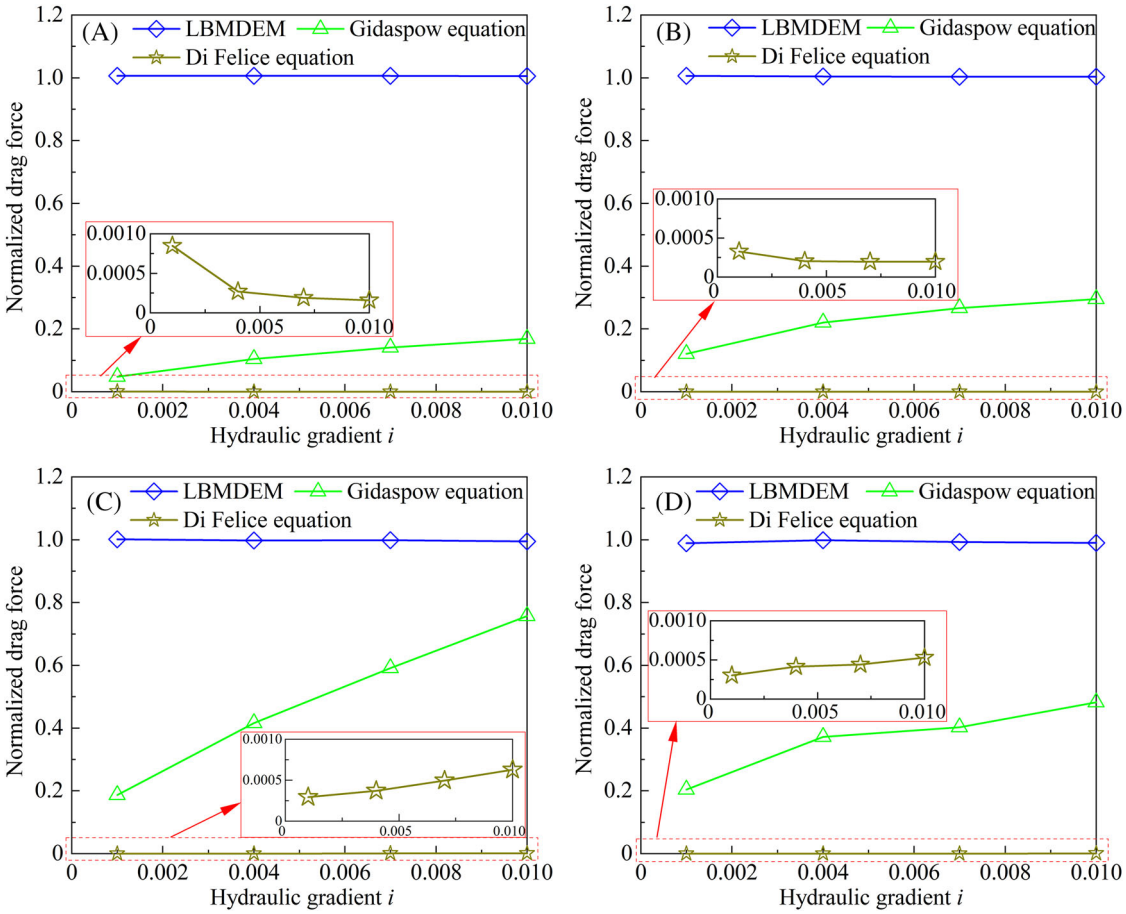

FIGURE 14 Variation of the normalized drag force with hydraulic gradient for the samples with various particle diameters of (A) 0.001 m, (B) 0.002 m, (C) 0.003 m and (D) 0.004 m

that the normalised drag force for LBMDEM simulations remain at about 1 for all the samples, suggesting that the drag forces in LBMDEM simulations are almost the same as the analytical values. By contrast, the drag forces using Gidaspow and Di Felice equations for all the samples are lower than the analytical values. In particular, the normalized drag force for the Di Felice equation is even close to zero. As the hydraulic gradient increases, the normalised drag force for the Gidaspow equation increases. For the samples with low particle diameters (smaller than 0.002 m), the normalised drag force for the Di Felice equation decreases with the increase of hydraulic gradient; on the contrary, for the samples with high particle diameters (larger than 0.003 m), the force is almost constant regardless of the hydraulic gradient applied.

To better observe the accuracy of empirical equations, the variation of the normalised drag force with porosity and particle diameter is shown in Figures 15 and 16, respectively. We can see the normalized drag force for LBMDEM is almost always 1, indicating that the high-resolution LBMDEM models can accurately simulate the drag force regardless of the porosity and particle diameter of the granular packing. However, it is found that there are remarkable errors in drag calculation by empirical equations. As the porosity and particle diameter increase, the normalized drag force for the Di Felice equation decreases. In other words, the drag force obtained by the Di Felice equation is much worse with the increase of porosity and particle diameter. By contrast, the error of drag force calculated by the Gidaspow equation increases with the increasing porosity and particle diameter.

6 | A NEW DRAG MODEL FOR 2D CASES

As discussed earlier, the prediction performances of the Gidaspow and Di Felice models are not satisfactory for 2D problems. However, they have been widely applied to 2D fluid-particle simulation (e.g.[44,45] due to the lack of better drag models for 2D simulations. In this work, based on our high-resolution simulations, we attempt to propose a drag model for

10969853, 0, Downloaded from https://onlinelibrary.wiley.com/doi/10.1002/nag.3496 by Test, Wiley Online Library on [10/02/2023]. See the Terms and Conditions (https://onlinelibrary.wiley.com/terms-and-conditions) on Wiley Online Library for rules of use; OA articles are governed by the applicable Creative Commons License

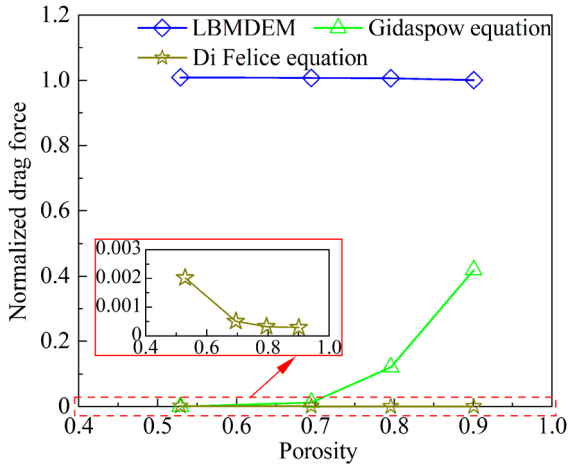

FIGURE 15 Variation of normalized drag force with porosity under a hydraulic gradient of 0.001

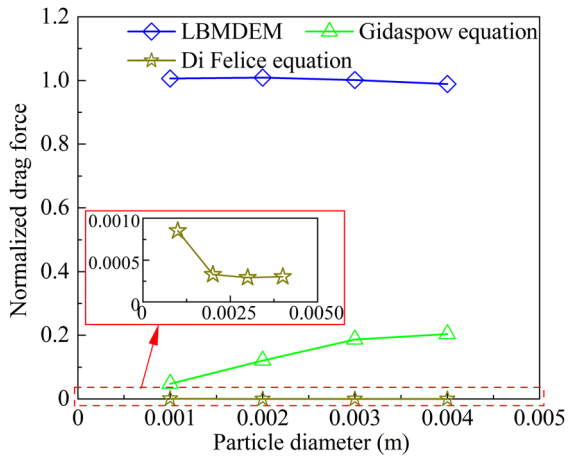

FIGURE 16 Variation of normalized drag force with particle diameter of samples with a porosity of 0.80 and under a hydraulic gradient of 0.001

geotechnical problems where dense particle packings are always encountered. Firstly, the drag forces in LBMDEM simulations for all the samples are calculated by removing the pressure gradient contribution according to Equation (22). The expected drag coefficient C_D are then derived from the drag force of each particle using the following equation[46]:

$$F_d = \frac{1}{2}\rho_f(\mathbf{U}-\mathbf{V})^2 d_p C_D \tag{22}$$

The variations of the obtained drag coefficient C_D with the porosity and Reynolds number are summarised in Figure 17. It appears that the obtained drag coefficient decreases with the increases of porosity and Reynolds number. The relationship between the obtained drag coefficient, porosity and Reynolds number can be described below with a squared correlation coefficient of 0.960:

$$C_D = 28.2087\, \emptyset_f^{-7.25} Re^{-1.00} \tag{23}$$

Based on Equation (22), the drag forces for all the samples are then calculated. The typical calculated results using the new model are compared with the simulation results using LBMDEM in Figure 18. On the whole, there is a good agreement between the estimation and the simulation, especially for the packing with a lower porosity, indicating the good performance of the proposed drag model for geotechnical problems where the dense granular packing with a low porosity is often encountered.

10969853, 0, Downloaded from https://onlinelibrary.wiley.com/doi/10.1002/nag.3496 by Test, Wiley Online Library on [10/02/2023]. See the Terms and Conditions (https://onlinelibrary.wiley.com/terms-and-conditions) on Wiley Online Library for rules of use; OA articles are governed by the applicable Creative Commons License

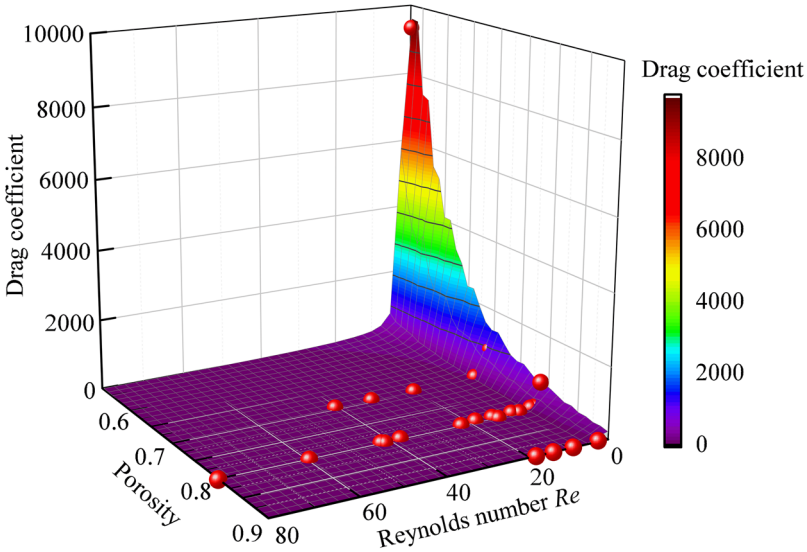

FIGURE 17 Variations of drag coefficient with porosity and Reynolds number

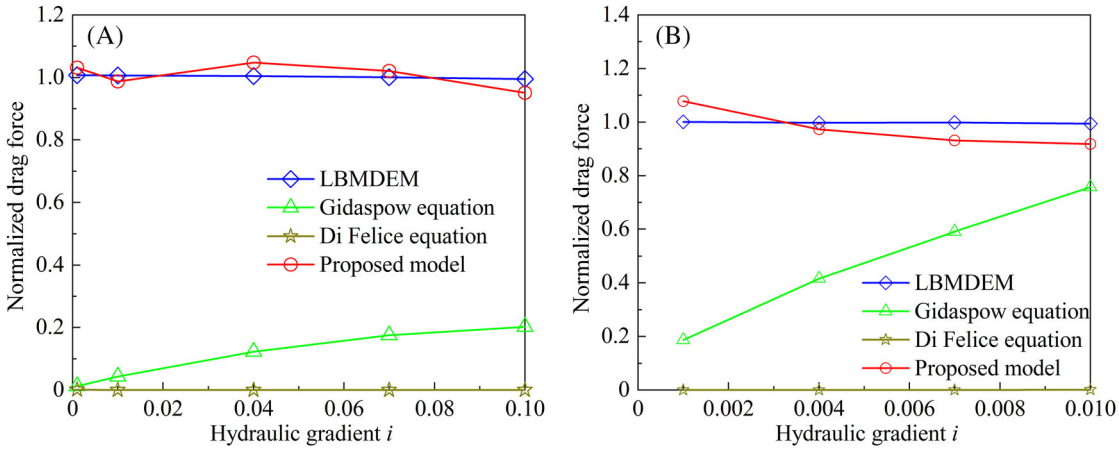

FIGURE 18 Comparison of drag forces between the proposed model and LBMDEM simulations. (A) The samples with particle diameter 0f 0.002 m and a porosity of 0.70, and (B) the samples with particle diameter 0f 0.003 m and a porosity of 0.80

7 | CONCLUSION

In this work, we have carried out a series of high-resolution LBMDEM simulations for fluid flows in granular particle packings with various porosities and particle diameters. Based on the high-resolution simulations (representative volume element models) for fluid flow, we further have calculated the hydrodynamic forces and drag forces applied to the particle packings at the steady state, and compared them with the analytical solutions and results obtained by LBMDEM modelling. The primary findings can be summarised as follows:

1. The high-resolution LBMDEM models can accurately simulate fluid-particle interactions for granular particle packings with various porosities and particle sizes. Particularly, from the LBMDEM simulations with porosity being less than 0.80, the hydrodynamic forces within the packing can be regarded as uniform distribution along the flow direction.
2. For most of the cases investigated in this work, the existing averaging-based empirical equations underestimate the hydrodynamic forces, and the numerical errors are dependent on porosity and particle size of the particle packing.
3. After decomposing the hydrodynamic force into a viscous drag force term and a pressure gradient-induced term, we find that the error of the existing empirical equations is mainly from the drag force term.
4. Based on the simulation results, a new drag force model is proposed. The numerical comparison conducted reveals a better performance of the proposed model than both Di Felice and Gidaspow models.

10969853, 0, Downloaded from https://onlinelibrary.wiley.com/doi/10.1002/nag.3496 by Test, Wiley Online Library on [10/02/2023]. See the Terms and Conditions (https://onlinelibrary.wiley.com/terms-and-conditions) on Wiley Online Library for rules of use; OA articles are governed by the applicable Creative Commons License

As the high-resolution CFDDEM model can accurately solve the fluid-particle interactions, but its huge computing cost hinders its application to large-scale problems under present computing capability. In contrast, the unresolved CFD-DEM based on the empirical equations for fluid-particle coupling is more practical for engineering problems in terms of computing efficiency. Therefore, improving existing averaging techniques or empirical equations by considering the meso-structure of particle packings is of great importance. To this end, the high-resolution or direct numerical simulations could provide us with an insightful perspective on the correction of averaging-based empirical equations. Notably, the packings with various particle size distributions were not considered in this study as the empirical equations only consider the whole hydrodynamic forces applied to the representative packing or element in the averaging technique. Certainly, the particle size distribution can have a significant effect on the pore curvature and it is a very complex and challenging problem to consider the particle size distribution in the empirical equations. We will try to address this issue in our following work.

DATA AVAILABILITY STATEMENT

Research data not shared.

ORCID

Zhixiong Zeng https://orcid.org/0000-0003-4255-8267
Jinlong Fu https://orcid.org/0000-0003-2964-4777
Min Wang https://orcid.org/0000-0002-4454-2480

REFERENCES

1. Batchelor GK. Sedimentation in a dilute dispersion of spheres. *J Fluid Mech*. 1972;52(2):245-268.
2. Tsuji Y, Kawaguchi T, Tanaka T. Discrete particle simulation of two-dimensional fluidized bed. *Powder Technol*. 1993;77(1):79-87.
3. Zhu HP, Zhou ZY, Yang RY, Yu AB. Discrete particle simulation of particulate systems: a review of major applications and findings. *Chem Eng Sci*. 2008;63(23):5728-5770.
4. Zhao J, Shan T. Coupled CFD–DEM simulation of fluid–particle interaction in geomechanics. *Powder Technol*. 2013;239:248-258.
5. Wang M, Feng YT, Pande GN, Chan AHC, Zuo WX. Numerical modelling of fluid-induced soil erosion in granular filters using a coupled bonded particle lattice Boltzmann method. *Comput Geotech*. 2017a;82:134-143.
6. Knight C, O'Sullivan C, van Wachem B, Dini D. Computing drag and interactions between fluid and polydisperse particles in saturated granular materials. *Comput Geotech*. 2020;117:103210.
7. Takagi S, Oguz HN, Zhang Z, Prosperetti A. PHYSALIS: a new method for particle simulation: part II: two-dimensional Navier–Stokes flow around cylinders. *J Comput Phys*. 2003;187(2):371-390.
8. Zeghal M, El Shamy U. A continuum-discrete hydromechanical analysis of granular deposit liquefaction. *Int J Numer Anal Methods Geomech*. 2004;28(14):1361-1383.
9. Akiki G, Moore WC, Balachandar S. Pairwise-interaction extended point-particle model for particle-laden flows. *J Comput Phys*. 2017a;351:329-357.
10. Wang M, Feng YT, Qu TM, Tao S, Zhao TT. Instability and treatments of the coupled discrete element and lattice Boltzmann method by the immersed moving boundary scheme. *Int J Numer Methods Eng*. 2020;121(21):4901-4919.
11. Zhang DZ, Prosperetti A. Averaged equations for inviscid disperse two-phase flow. *J Fluid Mech*. 1994;267:185-219.
12. Fox RO. A kinetic-based hyperbolic two-fluid model for binary hard-sphere mixtures. *J Fluid Mech*. 2019;877:282-329.
13. Balachandar S, Liu K, Lakhote M. Self-induced velocity correction for improved drag estimation in Euler–Lagrange point-particle simulations. *J Comput Phys*. 2019;376:160-185.
14. Uhlmann M. An immersed boundary method with direct forcing for the simulation of particulate flows. *J Comput Phys*. 2005;209(2):448-476.
15. Feng YT, Han K, Owen DRJ. Coupled lattice Boltzmann method and discrete element modelling of particle transport in turbulent fluid flows: computational issues. *Int J Numer Methods Eng*. 2007;72(9):1111-1134.
16. Zou YH, Chen Q, Chen XQ, Cui P. Discrete numerical modeling of particle transport in granular filters. *Comput Geotech*. 2013;47:48-56.
17. Shan T, Zhao J. A coupled CFD-DEM analysis of granular flow impacting on a water reservoir. *Acta Mech*. 2014;225(8):2449-2470.
18. Zhao T, Dai F, Xu NW. Coupled DEM-CFD investigation on the formation of landslide dams in narrow rivers. *Landslides*. 2017;14(1):189-201.
19. Hu Z, Zhang Y, Yang Z. Suffusion-induced evolution of mechanical and microstructural properties of gap-graded soils using CFD-DEM. *J Geotech Geoenviron Eng*. 2020;146(5):04020024.
20. Liu Y, Yin ZY, Wang L, Hong Y. A coupled CFD–DEM investigation of internal erosion considering suspension flow. *Can Geotech J*. 2021;58(9):1411-1425.
21. Qian JG, Zhou C, Yin ZY, Li WY. Investigating the effect of particle angularity on suffusion of gap-graded soil using coupled CFD-DEM. *Comput Geotech*. 2021a;139:104383.

10969853, 0, Downloaded from https://onlinelibrary.wiley.com/doi/10.1002/nag.3496 by Test, Wiley Online Library on [10/02/2023]. See the Terms and Conditions (https://onlinelibrary.wiley.com/terms-and-conditions) on Wiley Online Library for rules of use; OA articles are governed by the applicable Creative Commons License

22. Qian JG, Li WY, Yin ZY, Yang Y. Influences of buried depth and grain size distribution on seepage erosion in granular soils around tunnel by coupled CFD-DEM approach. *Transp Geotech*. 2021b;29:100574.
23. Di Felice R. The voidage function for fluid-particle interaction systems. *Intl J Multiphase Flow*. 1994;20:153-159.
24. Akiki G, Jackson TL, Balachandar S. Pairwise interaction extended point-particle model for a random array of monodisperse spheres. *J Fluid Mech*. 2017b;813:882-928.
25. Zhang DZ, VanderHeyden WB. The effects of mesoscale structures on the macroscopic momentum equations for two-phase flows. *Int J Multiphase Flow*. 2002;28(5):805-822.
26. Zhang Z, Prosperetti A. A second-order method for three-dimensional particle simulation. *J Comput Phys*. 2005;210(1):292-324.
27. Cheng K, Wang Y, Yang Q. A semi-resolved CFD-DEM model for seepage-induced fine particle migration in gap-graded soils. *Comput Geotech*. 2018;100:30-51.
28. Kanitz M, Grabe J. The influence of the void fraction on the particle migration: a coupled computational fluid dynamics–discrete element method study about drag force correlations. *Int J Numer Anal Methods Geomech*. 2021;45(1):45-63.
29. Abdi R, Krzaczek M, Tejchman J. Comparative study of high-pressure fluid flow in densely packed granules using a 3D CFD model in a continuous medium and a simplified 2D DEM-CFD approach. *Granular Matter*. 2022;24(1):1-25.
30. Third JR, Chen Y, Müller CR. Comparison between finite volume and lattice-Boltzmann method simulations of gas-fluidised beds: bed expansion and particle–fluid interaction force. *Comput Part Mech*. 2016;3(3):373-381.
31. Cheng K, Zhang C, Peng K, Liu H, Ahmad M. Un-resolved CFD-DEM method: an insight into its limitations in the modelling of suffusion in gap-graded soils. *Powder Technol*. 2021;381:520-538.
32. Zhang Y, Li Y, Gao Z, et al. Effects of drag force correlations on the mixing and segregation of polydisperse gas-solid fluidized bed by CFD-DEM simulation. *Can J Chem Eng*. 2019;97:1708-1717.
33. Gidaspow D. *Multiphase flow and fluidization: continuum and kinetic theory descriptions*. Academic Press; 1994.
34. Sarkar S, van der Hoef MA, Kuipers JAM. Fluid–particle interaction from lattice Boltzmann simulations for flow through polydisperse random arrays of spheres. *Chem Eng Sci*. 2009;64(11):2683-2691.
35. Cello F, Di Renzo A, Di Maio FP. A semi-empirical model for the drag force and fluid–particle interaction in polydisperse suspensions. *Chem Eng Sci*. 2010;65(10):3128-3139.
36. Rong LW, Dong KJ, Yu AB. Lattice-Boltzmann simulation of fluid flow through packed beds of spheres: effect of particle size distribution. *Chem Eng Sci*. 2014;116:508-523.
37. Wang T, Zhang F, Furtney J, Damjanac B. A review of methods, applications and limitations for incorporating fluid flow in the discrete element method. *J Rock Mech Geotech Eng*. 2022. doi:10.1016/j.jrmge.2021.10.015
38. Noble DR, Torczynski JR. A lattice-Boltzmann method for partially saturated computational cells. *Int J Mod Phys C*. 1998;9(08):1189-1201.
39. Wang M, Feng YT, Owen DRJ, Qu TM. A novel algorithm of immersed moving boundary scheme for fluid–particle interactions in DEM–LBM. *Comput Meth Appl Mech Eng*. 2019;346:109-125.
40. Wang M, Feng YT, Wang CY. Coupled bonded particle and lattice Boltzmann method for modelling fluid–solid interaction. *Int J Numer Anal Methods Geomech*. 2016;40(10):1383-1401.
41. Wang M, Feng YT, Wang CY. Numerical investigation of initiation and propagation of hydraulic fracture using the coupled Bonded Particle–Lattice Boltzmann Method. *Comput Struct*. 2017b;181:32-40.
42. Wang M, Yang Y, Zhang DZ, Balachandar S. Numerical calculation of the particle–fluid–particle stress in random arrays of fixed particles. *Phys Rev Fluids*. 2021;6(10):104306.
43. van der Hoef MA, Beetstra R, Kuipers JAM. Lattice-Boltzmann simulations of lowReynolds-number flow past mono- and bidisperse arrays of spheres: results for the permeability and drag force. *J Fluid Mech*. 2005;528:233-254. http://www.journals.cambridge.org/abstract_S0022112004003295
44. Chu KW, Wang Y, Zheng QJ, Yu AB, Pan RH. CFD-DEM study of air entrainment in falling particle plumes. *Powder Technol*. 2020;361:836-848.
45. Guo R, Bai J, Wu F, Wang J, Ma X, Hui Z. CFD–DEM simulation of wet granular-fluid flows and heat transfer in an integral multi-jet spout-fluidized bed. *Powder Technol*. 2022;403:117384.
46. Zwick D, Balachandar S. A scalable Euler–Lagrange approach for multiphase flow simulation on spectral elements. *Int J High Perform Comput Appl*. 2020;34(3):316-339.

How to cite this article: Zeng Z, Fu J, Feng YT, Wang M. Revisiting the empirical particle-fluid coupling model used in DEM-CFD by high-resolution DEM-LBM-IMB simulations: A 2D perspective. *Int J Numer Anal Methods Geomech*. 2023;1-18. https://doi.org/10.1002/nag.3496

10969853, 0, Downloaded from https://onlinelibrary.wiley.com/doi/10.1002/nag.3496 by Test, Wiley Online Library on [10/02/2023]. See the Terms and Conditions (https://onlinelibrary.wiley.com/terms-and-conditions) on Wiley Online Library for rules of use; OA articles are governed by the applicable Creative Commons License